International Journal of Heat and Mass Transfer 52 (2009) 5533–5546

Contents lists available at ScienceDirect

International Journal of Heat and Mass Transfer

journal homepage: www.elsevier.com/locate/ijhmt

Formation of weld crater in GMAW of aluminum alloys

H. Guo [a], J. Hu [b,*], H.L. Tsai [a]

[a] Department of Mechanical and Aerospace Engineering, Missouri University of Science and Technology (formerly University of Missouri – Rolla), 400 W. 13th Street, Rolla, MO 65409, USA
[b] Department of Mechanical Engineering, University of Bridgeport, Bridgeport, CT 06604, USA

ARTICLE INFO

Article history:
Received 9 October 2008
Received in revised form 17 June 2009
Accepted 17 June 2009
Available online 5 August 2009

Keywords:
GMAW
Aluminum Welding
Crater
Microstructure

ABSTRACT

Both mathematical modeling and experiments have been conducted on the formation of the crater formed in a GMAW of aluminum alloy 6005-T4. Transient weld pool shape and the distributions of temperature and velocity were calculated by a three-dimensional numerical model. The final weld bead shape and dimensions were obtained. Corresponding experiments were conducted and in good agreement with modeling predictions. Metallurgical characterizations were also performed on the experimental samples. It was found that due to the fast solidification of the weld pool after the termination of the welding arc, there is no time for the molten metal to flow back towards the weld pool center and close up the crater. Thus a crater was formed at the end of the weld bead. Solidification cracking was formed at the center of weld crater. A "back-up" technique was proposed to allow extra molten metal to flow back to the crater and fill it up. The crater was successfully filled and the crater cracking was eliminated.

1. Introduction

Gas metal arc welding (GMAW) is an arc welding process which uses a metal wire as a combined electrode and filler metal in a plasma arc of inert shielding gas. Filler metal is added to the weld pool automatically and continuously. GMAW has some advantages over other welding methods, such as high productivity, better penetration, no need for flux, little spatter, and ability to weld in all positions. Therefore, it has been one of the most popular welding methods in industry. Due to the demands for a lower environmental impact through improved fuel efficiency, weight reduction, and load capacity, aluminum is being more and more widely used in the auto industry because of its light weight. More automobile body structures, such as engine cradles, are being manufactured with aluminum instead of steel.

One feature of these aluminum welds is that they are much shorter than normal welds. They are usually less than 10 cm in length, and many are only around three or four centimeters. Therefore, the terminating end (weld crater) makes up a great portion of short welds (Fig. 1). At the crater, the welding arc and wire feed are terminated. Unlike the middle portion of a long weld, where the welding process is in a quasi-steady state, the energy, mass and momentum transfer varies sharply from moment to moment in a cold weld, thus creating very unsteady temperature and fluid flow fields. For GMAW of aluminum, the weld pool solidifies very fast due to the very high heat conductivity of aluminum alloys, leading to the formation of cracking, which is a major defect in weld craters. Cracks are likely to occur where the metal lacks ductility and the tensile stress develops after the shut off of heat and mass input at the end of the welding process [1,2].

Hot cracking occurs when metal is above solidus temperature and a tensile stress is applied [2,3]. It usually happens when welding the heat-treatable aluminum alloys, resulting from the use of incorrect filler metal, excessive base alloy dilution of a weld, an improper joint design or excessive joint spacing [2]. Aluminum alloys are sensitive to solidification cracking as a result of high thermal expansion combined with a brittle structure at and just below the solidification temperature [4]. According to the studies of Pereira et al. [5], the development of fine grain structure in the weldment helps to reduce the solidification cracking tendency. The shape of the weld pool also plays an important role in the development of solidification cracking. The liquation cracking in the HAZ was investigated by Kerr and Katoh [6]. The crack length increased linearly with the increase of augmented strain or the heat input. The simulation of liquation cracking in 7017 aluminum alloy [7] found it is determined by both the applied stress level and the temperature at which stress is applied. Increasing the cooling rate may minimize the cracking. The relationships between the restraint intensity of weld grooves in aluminum alloy and hot cracking of weld metals were investigated [8]. To prevent cracking, the welding parameters should be selected carefully to obtain a proper cross-sectional shape of the weld bead [8].

Numerous studies have been carried out on the welding process, but no detailed analysis has been reported on crater in gas metal arc welding of aluminum alloys. Many experimental studies

---

* Corresponding author. Tel.: +1 203 576 4757; fax: +1 203 576 4765.
E-mail address: jjhu@bridgeport.edu (J. Hu).

0017-9310/$ - see front matter © 2009 Elsevier Ltd. All rights reserved.
doi:10.1016/j.ijheatmasstransfer.2009.06.028

Nomenclature

c	specific heat
f	mass fraction
g	gravitational acceleration
h	enthalpy
h_c	convective heat transfer coefficient
k	thermal conductivity
$\vec{\boldsymbol{n}}$	normal vector to the local surface
p	pressure
p_v	vapor pressure or any other applied external pressure
r–z	cylindrical coordinate system
$\vec{\boldsymbol{s}}$	local surface tangential vector
t	time
u	velocity in x-direction
u_w	arc voltage
v	velocity in y-direction
w	velocity in z-direction
$\boldsymbol{B}$	magnetic induction vector
C	inertial coefficient
D	mass diffusion coefficient
F	volume of fluid function
H_v	latent heat of vaporization
I	welding current
$\vec{\boldsymbol{J}}$	current density vector
K	permeability function
P_{max}	maximum arc pressure at the arc center
T	temperature
$\vec{\boldsymbol{V}}$	velocity vector
$\vec{\boldsymbol{V}}_r$	relative velocity vector between the liquid phase and solid phase.
W	melt mass evaporation rate

Greek symbols

β_T	thermal expansion coefficient
γ	surface tension coefficient
ε	surface radiation emissivity
κ	free surface curvature
η	arc thermal efficiency
η_d	ratio of droplet thermal energy to the total arc energy
σ	Stefan–Boltzmann constant
ρ	density
μ	dynamic viscosity
σ_p	arc pressure distribution parameter
σ_q	arc heat flux distribution parameter
$\tau_{\vec{s}}$	Marangoni shear stress

Subscripts

0	initial condition
d	droplet
l	liquid phase
m	melting point of aluminum
s	solid phase

have been conducted on the GMAW process [9–16]. Since GMAW is a very complicated process involving many coupled parameters, such as welding current, voltage, welding speed, electrode feed speed, base metal material, electrode material, electrode size, and shielding gas, and also because welding is a transient process at high temperatures, it is very hard to use experimental methods alone to understand its mechanisms. Mathematical modeling provides a convenient way to get insightful information. Many studies have been performed on the mathematical modeling of the welding process in the past. It was found that fluid flow within the weld pool is driven by forces such as buoyancy, electromagnetic forces, surface tension, and arc plasma drag forces. Effect of gravity on weld pool shape was simulated. A high gravitational field causes an enhanced buoyancy-driven radially outward flow in the weld pool [17]. Surface tension is one of the major driving forces [18–23]. Electromagnetic forces drive fluid in a downward motion and cause a deeper penetration [18,24]. In the welding process the arc plasma drag force induces an outward fluid flow on the weld pool surface [21].

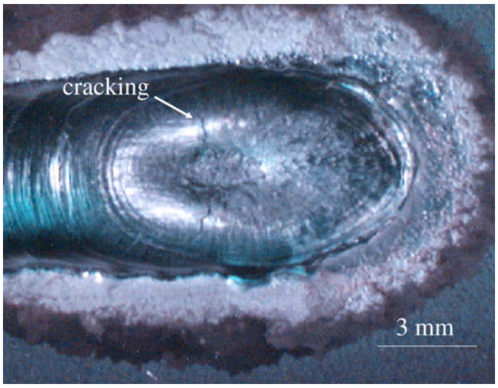

Fig. 1. A crater with cracking at the end of a weld.

Since the middle of the 1980s, many theoretical models have been established on the simulation of the gas metal arc welding process. Ushio and Wu proposed a model to calculate the three-dimensional heat and fluid flow in a moving gas metal arc weld pool [25]. A boundary-fitted nonorthogonal coordinate system was adopted and it was found that the size and profile of the weld pool are strongly influenced by the volume of molten wire, impact of droplets, and heat content of droplets [25]. A flat weld pool surface is assumed in Jaidi and Dutta [26]. Park and Rhee reported that the kinetic energy of the transferring droplets produces a depression on the weld pool surface [27]. According to the computational investigations by Davies et al. [28], the impinging droplet momentum dominates the flow pattern and overrides any surface tension effects at a relatively high current. Arghode et al. [29] simulated the effect of molten droplet addition to the weld pool as volumetric heat and species sources. Wang and Tsai [23] and Hu and Tsai [30–33] developed detailed models on the impingement of filler droplets and weld pool dynamics and calculated the combined effect of droplet impingement and surface tension. However, all the research efforts were focused only on the quasi-steady state part of the GMAW process.

The objectives of this project are to obtain a better understanding of the formation mechanism of crater and to find a proper improvement procedure. The fluid flow and heat transfer were calculated when droplet carries mass, momentum, and thermal energy into the weld pool. The transient deformed weld pool surface was handled by the volume of fluid (VOF) technique [34] and the fusion and solidification in the liquid region, the mushy zone and the solid region were handled by the continuum formulation [35]. In experimental research, bead-on-plate experiments were performed. Experimental samples were then characterized using metallurgraphical methods.

2. Mathematical model

A sketch of a moving GMAW for a plate is shown in Fig. 1. The three-dimensional x–y–z-coordinate system is fixed to the base metal. The arc is moving in the positive *x*-direction, and droplets impinge onto the base metal in the negative *z*-direction while moving at the same velocity along the *x*-direction as the arc.

2.1. Governing equations

The differential equations governing the conservation of mass, momentum, and energy based on continuum formulation given by Diao and Tsai [35] were modified and employed in the study. The equations are given below:

(1) Continuity,

$$\frac{\partial\rho}{\partial t}+\nabla\cdot\left(\rho\vec{\boldsymbol{V}}\right)=0. \tag{1}$$

(2) Momentum,

$$\begin{aligned}\frac{\partial}{\partial t}(\rho u)+\nabla\cdot\left(\rho\vec{\boldsymbol{V}}u\right)=&\nabla\cdot\left(\mu_l\frac{\rho}{\rho_l}\nabla u\right)-\frac{\partial p}{\partial x}-\frac{\mu_l}{K}\frac{\rho}{\rho_l}(u-u_s)\\&-\frac{C\rho^2}{K^{1/2}\rho_l}|u-u_s|(u-u_s)\\&-\nabla\cdot\left(\rho f_s f_l\underset{r}{\vec{\boldsymbol{V}}}u_r\right)+\vec{\boldsymbol{J}}\times\vec{\boldsymbol{B}}|_x,\end{aligned} \tag{2}$$

$$\begin{aligned}\frac{\partial}{\partial t}(\rho v)+\nabla\cdot\left(\rho\vec{\boldsymbol{V}}v\right)=&\nabla\cdot\left(\mu_l\frac{\rho}{\rho_l}\nabla v\right)-\frac{\partial p}{\partial y}-\frac{\mu_l}{K}\frac{\rho}{\rho_l}(v-v_s)\\&-\frac{C\rho^2}{K^{1/2}\rho_l}|v-v_s|(v-v_s)\\&-\nabla\cdot\left(\rho f_s f_l\underset{r}{\vec{\boldsymbol{V}}}v_r\right)+\vec{\boldsymbol{J}}\times\vec{\boldsymbol{B}}|_y,\end{aligned} \tag{3}$$

$$\begin{aligned}\frac{\partial}{\partial t}(\rho w)+\nabla\cdot\left(\rho\vec{\boldsymbol{V}}w\right)=&\nabla\cdot\left(\mu_l\frac{\rho}{\rho_l}\nabla w\right)-\frac{\partial p}{\partial z}-\frac{\mu_l}{K}\frac{\rho}{\rho_l}(w-w_s)\\&-\frac{C\rho^2}{K^{1/2}\rho_l}|w-w_s|(w-w_s)\\&-\nabla\cdot\left(\rho f_s f_l\underset{r}{\vec{\boldsymbol{V}}}w_r\right)+\rho g+\rho g(\beta_T(T-T_0)\\&+\beta_s\left(f_l^\alpha-f_{l,0}^\alpha\right)\Big)+\vec{\boldsymbol{J}}\times\vec{\boldsymbol{B}}|_z+F_{drag}.\end{aligned} \tag{4}$$

(3) Energy,

$$\begin{aligned}\frac{\partial}{\partial t}(\rho h)+\nabla\cdot\left(\rho\vec{\boldsymbol{V}}h\right)=&\nabla\cdot\left(\frac{k}{c_s}\nabla h\right)+\nabla\cdot\left(\frac{k}{c_s}\nabla(h_s-h)\right)\\&-\nabla\cdot\left(\rho\left(\vec{\boldsymbol{V}}-\underset{s}{\vec{\boldsymbol{V}}}\right)(h_l-h)\right).\end{aligned} \tag{5}$$

(4) Species,

$$\begin{aligned}\frac{\partial}{\partial t}(\rho f^\alpha)+\nabla\cdot\left(\rho\vec{\boldsymbol{V}}f^\alpha\right)=&\nabla\cdot(\rho D\nabla f^\alpha)+\nabla\cdot(\rho D\nabla(f_l^\alpha-f^\alpha))\\&-\nabla\cdot\left(\rho\left(\vec{\boldsymbol{V}}-\underset{s}{\vec{\boldsymbol{V}}}\right)(f_l^\alpha-f^\alpha)\right),\end{aligned} \tag{6}$$

where t is the time; ρ is the density; $\vec{\boldsymbol{V}}$ is the velocity vector; u, v and w are the velocities in the x-, y-, and z-directions, respectively; $\underset{r}{\vec{\boldsymbol{V}}}=\underset{l}{\vec{\boldsymbol{V}}}-\underset{s}{\vec{\boldsymbol{V}}}$ is the relative velocity vector between the liquid phase and the solid phase; the subscripts s and l refer to the solid and liquid phases, respectively; p is the pressure; μ is the dynamic viscosity; f is the mass fraction; K is the permeability, a measure of the ease with which fluids pass through the porous mushy zone; C is the inertial coefficient; β_T is the thermal expansion coefficient; g is the gravitational acceleration; T is the temperature; $\vec{\boldsymbol{B}}$ is the magnetic induction vector; $\vec{\boldsymbol{J}}$ is the current density vector; the subscript 0 represents the initial condition; h is the enthalpy; k is the thermal conductivity; c is the specific heat; f_α is the fraction of constituent; and D is the mass diffusivity. The detailed descriptions of the terms in Eqs. (1)–(5) can be found in Refs. [23,30–33] and will not be repeated here. The solid/liquid phase-change is handled by the continuum formulation [35]. The third, fourth and fifth terms in the right-hand side of Eqs. (2)–(4) vanish at the solid region because of $u = u_s = v = v_s = w = w_s = 0$ and $f_l = 0$ for the solid. In the liquid region, K goes to infinity, and all these terms also vanish [23,30–33]. Those terms are only effective for the mushy zone where $0 < f_l < 1$ and $0 < f_s < 1$. Therefore, the liquid region, mushy zone and solid region can be handled by the same equations. During the fusion and solidification process, latent heat is absorbed or released in the mushy zone.

2.2. Tracking of free surfaces

Volume of fluid (VOF) technique [34] was employed to track the dynamic free surfaces. The fluid configuration is defined by a volume of fluid function, $F(x, y, z, t)$, which represents the volume of liquid metal per unit volume and satisfies the following conservation equation:

$$\frac{dF}{dt}=\frac{\partial F}{\partial t}+(\vec{\boldsymbol{V}}\cdot\nabla)F=0. \tag{7}$$

When averaged over the cells of a computing mesh, the average value of F in a cell is equal to the fractional volume of the cell occupied by fluid. A unit value of F corresponds to a cell full of fluid, whereas a zero value indicates a cell contains no fluid. Cells with F values between zero and one are partially filled with fluid and identified as surface cells.

2.3. Boundary conditions

The boundary conditions for the previous Eqs. (1)–(6) are given below.

2.3.1. Normal to the local free surface

For cells containing a free surface, that is, cells that contain fluid but have one or more empty neighbors, the following pressure conditions must be satisfied [34]:

$$p=p_v+\gamma\kappa, \tag{8}$$

where p is the pressure at the free surface in a direction normal to the local free surface and p_v is the plasma arc pressure which is assumed to have a radial distribution in the following form [25]:

$$p_v=P_{max}\exp\left(-\frac{r^2}{2\sigma_p^2}\right), \tag{9}$$

where P_{max} is the maximum arc pressure at the arc center, which is calculated from the welding current [25], r is the distance from the arc center, and σ_p is the arc pressure distribution parameter [25]. κ in Eq. (8) is the free surface curvature given by

$$\kappa=-\left[\nabla\cdot\left(\frac{\vec{\boldsymbol{n}}}{|\vec{\boldsymbol{n}}|}\right)\right]=\frac{1}{|\vec{\boldsymbol{n}}|}\left[\left(\frac{\vec{\boldsymbol{n}}}{|\vec{\boldsymbol{n}}|}\cdot\nabla\right)|\vec{\boldsymbol{n}}|-\left(\nabla\cdot\vec{\boldsymbol{n}}\right)\right], \tag{10}$$

where $\vec{\boldsymbol{n}}$ is the normal vector to the local surface, which is the gradient of VOF function $\vec{\boldsymbol{n}}=\nabla F$.

2.3.2. Tangential to the local free surface

The Marangoni shear stress at the free surface in a direction tangential to the local free surface is given by

$$\tau_{\vec{s}} = \mu_l \frac{\partial\left(\vec{\boldsymbol{V}}\cdot\vec{\boldsymbol{s}}\right)}{\partial\vec{\boldsymbol{n}}} = \frac{\partial\gamma}{\partial T}\frac{\partial T}{\partial\vec{\boldsymbol{s}}}, \tag{11}$$

where $\vec{\boldsymbol{s}}$ is the local surface tangential vector. Since there is no surface tension coefficient data available for 6005-T4, the property of pure aluminum was used instead. For pure aluminum, surface tension coefficient γ is a function of temperature [36].

$$\gamma = 868 - 0.152(T - T_m), \tag{12}$$

where T is the temperature and T_m is the melting temperature of aluminum.

2.3.3. Top surface

At the moving arc center, in addition to the droplet impingement, arc heat flux is also impacting on the base metal. Since the arc heat flux is relatively concentrated, it is assumed that the heat flux is perpendicular to the base metal (i.e., neglecting the inclination of current and heat flux). Therefore, the temperature boundary conditions at the top surface of the base metal are

$$k\frac{\partial T}{\partial z} = \frac{\eta(1-\eta_d)Iu_w}{2\pi\sigma_q^2}\exp\left(-\frac{r^2}{2\sigma_q^2}\right) - q_{conv} - q_{radi} - q_{evap}, \tag{13}$$

where I is the welding current, η is the arc thermal efficiency, η_d is the ratio of droplet thermal energy to the total arc energy, u_w is the arc voltage, and σ_q is the arc heat flux distribution parameter [20]. The heat loss due to convection, radiation, and evaporation can be written as

$$q_{conv} = h_c(T - T_\infty), \quad q_{radi} = \sigma\varepsilon(T^4 - T_\infty^4), \quad q_{evap} = WH_v, \tag{14}$$

where h_c is the convective heat transfer coefficient [20], T_∞ is the room temperature, σ is Stefan–Boltzmann constant, ε is the surface radiation emissivity [36], H_v is the latent heat for the liquid–vapor phase-change [37], and W is the melt mass evaporation rate [38].

2.3.4. Symmetrical y = 0 plane

$$\frac{\partial T}{\partial y} = 0; \quad \frac{\partial u}{\partial y} = 0; \quad v = 0; \quad \frac{\partial w}{\partial y} = 0; \quad \frac{\partial f^\alpha}{\partial y} = 0. \tag{15}$$

2.3.5. Other surfaces

$$-k\frac{\partial T}{\partial\vec{\boldsymbol{n}}} = q_{conv}; \quad u = 0; \quad v = 0; \quad w = 0. \tag{16}$$

2.4. Electromagnetic force

In Eqs. (2)–(4), there are three terms caused by the electromagnetic force, $\boldsymbol{J}\times\boldsymbol{B}$, which should be calculated first before the calculation of velocity. Assuming the electric field is a quasi-steady-state and the electrical conductivity is constant, the scalar electric potential, ϕ, satisfies the following Maxwell equation [22] in the local r–z-coordinate system:

$$\nabla^2\phi = \frac{1}{r}\frac{\partial}{\partial r}\left(r\frac{\partial\phi}{\partial r}\right) + \frac{\partial^2\phi}{\partial z^2} = 0. \tag{17}$$

The required boundary conditions for the solution of Eq. (17) are

$$-\sigma_e\frac{\partial\phi}{\partial z} = \frac{I}{2\pi\sigma_c^2}\times\exp\left(-\frac{r^2}{2\sigma_c^2}\right), \qquad \text{at the top free surface}, \tag{18}$$

$$\frac{\partial\phi}{\partial z} = 0, \qquad \text{at } z = 0, \tag{19}$$

$$\frac{\partial\phi}{\partial r} = 0, \qquad \text{at } r = 0, \tag{20}$$

$$\phi = 0, \qquad \text{at } r = 10\sigma_c, \tag{21}$$

where σ_e is the electrical conductivity and σ_c is the arc current distribution parameter [22]. After the distribution of electrical potential is solved, the current density in the r- and z-directions can be calculated via

$$J_r = -\sigma_e\frac{\partial\phi}{\partial r}; \quad J_z = -\sigma_e\frac{\partial\phi}{\partial z}. \tag{22}$$

The self-induced azimuthal magnetic field is derived from Ampere's law via the following equation [22]:

$$B_\theta = \frac{\mu_0}{r}\int_0^r J_z r\,dr, \tag{23}$$

where μ_0 is the magnetic permeability in free space. Finally, the three components of electromagnetic force in Eqs. (2)–(4) are calculated via the following equations [22]:

$$\vec{\boldsymbol{J}}\times\vec{\boldsymbol{B}}|_x = -B_\theta J_z\frac{x - x_a}{r}; \quad \vec{\boldsymbol{J}}\times\vec{\boldsymbol{B}}|_y = -B_\theta J_z\frac{y}{r}; \quad \vec{\boldsymbol{J}}\times\vec{\boldsymbol{B}}|_z = B_\theta J_r. \tag{24}$$

2.5. Numerical considerations

The governing equations were solved iteratively at each time step using finite volume method [39]. At each time step, the continuity and momentum equations were solved iteratively with a two-step projection method involving the time discretization of the momentum equations to get the velocity and pressure distributions [23]. Then the energy equation was solved explicitly to obtain the enthalpy and temperature field. The species equation was solved in a similar way. This process was repeated for each iteration step. Iteration within a time step was terminated when the solutions of velocity, pressure, temperature, and species distributions converged. Then the VOF function equation was solved to obtain the new free surface and liquid pool domain. The temperature-dependent material properties were updated. The time step was then advanced and the above procedure was repeated until the desired time was reached.

Since the governing equations are valid for the entire computational domain including the liquid phase, the solid phase, and the mushy zone, there is no need to track the shape and extent of each phase. Therefore, a fixed grid system was used in the calculation with refined grid cells in the weld pool zone to improve accuracy. Due to the symmetry of the x–z plane of the domain, a grid system of 408 × 66 × 56 points was used for the half computational domain to save computational time. The finer grids, concentrating on and around the weld pool, move with the weld pool as the welding proceeds. Time step length varied during the calculation to ensure the convergence and save computational time. The computation was performed on the Dell Precision 650® workstations with 3.2 GHz Pentium® 4 processors. It took about 71 h of CPU time to simulate 1.4 s of real-time welding. The average time step is around 2×10^{-5} s.

2.6. Material properties in simulation

The thermophysical properties shown in Table 1 were inputs into the numerical simulation model. When temperature-dependent material properties at high temperature were not available, constant values for the solid metal at room temperature were used.

Table 1
Thermophysical properties used in the model.

Property, unit	Value
Specific heat of solid phase, J/kg-K	900[a]
Specific heat of liquid phase, J/kg-K	900[a]
Thermal conductivity of solid phase, W/m-K	167[b]
Thermal conductivity of liquid phase, W/m-K	167[b]
Density of solid phase, kg/m^3	2700[b]
Density of liquid phase, kg/m^3	2300[b]
Coefficient of thermal expansion, K^{-1}	2.34×10^{-5}[b]
Dynamic viscosity, kg/m-s	0.0012[a]
Heat of fusion, J/kg	0.397[a]
Heat of vaporization, J/kg	1.08×10^{-7}[a]
Solidus temperature, K	880[b]
Liquidus temperature, K	927[b]
Electrical conductivity, $\Omega^{-1}\ m^{-1}$	2.5×10^{7}[b]
Plasma density, kg/m	0.06[b]
Plasma viscosity, kg/m-s	2.5×10^{-4}[b]

[a] Property of pure aluminum [36].
[b] Property of 6005 [40].

3. Experiments

3.1. Experimental setup

The experimental setup is shown in Fig. 2. In the experiments, bead-on-plate welds were made on aluminum alloy 6005-T4 plates 203.2 mm × 38.1 mm × 5 mm in dimension, which were extruded by Hydro Raufoss Automotive. Every weld coupon was chemically cleaned and degreased. The electrode material was 4043 produced by Alcoa. The diameter of the electrode wire was 1.6 mm in all experiments.

The welding machine was a Lincoln PowerWave 455® programmable waveform controlled welding machine made by Lincoln Electric. The weld torch was fixed onto a small cart on a rail. The travel speed of the cart could be adjusted. Argon was used as the protecting gas, which has a flow rate of 40 CFH. To provide an adequate protection of the weld pool, a welding gun leading angle of 15° was used in the experiments. The weld bead was made under constant current mode of the welding machine at the center of the plate along the *x*-direction as shown in Fig. 2. All welds started from 30 mm to the left end of the weld coupon. Before welding, the upper surface of the plate was brushed with a stainless steel brush to remove the oxide layer. Three major parameters could be adjusted during the process: welding current, wire feed speed, and arc/cart travel speed. Arc voltage was automatically set by the machine once other parameters were fixed.

3.2. Monitoring the welding process

It is very important that the experiments are closely monitored during the process by connecting the port on the PowerWave455® front panel to the serial port of a computer and using WaveDesigner® software from Lincoln Electric. The welding parameters, such as arc current, voltage, and welding time, were stored in the computer and input into the mathematical model later on.

3.3. Metallurgical characterizations of samples

3.3.1. Sample preparation

Welded samples were sectioned, grinded, polished, and then etched for metallurgical characterizations. Sectioning was performed on a Leco CM-15® cut-off machine. Coolant was used during the cutting process. The sectioned samples were hot mounted using Bakelite powder. The sample grinding and polishing were performed on a Leco Spectrum System2000® grinder/polisher. In grinding, 240-, 400-, 600-, 800-, and 1200-grit abrasive disks were used consecutively, and in polishing, diamond compounds of 6, 3, and 1 μm and 0.05 μm gamma alumina solution were used. The polished samples were then etched by Tucker's reagent and Keller's reagent [41] for macroscopy and microscopy analysis, respectively.

3.3.2. Metallurgical characterizations

Metallographic analysis was performed under stereoscopes and optical microscopes. An image acquisition system including a digital camera and a computer was used to capture and store the images. Adobe Photoshop® and Image Processing Tool Kit® were used for the processing of sample images. The weld penetration, width, and reinforcement were measured.

4. Results and discussion

4.1. Normal weld

The formation of the crater for GMAW of 6005-T4 aluminum alloy was calculated. The fluid flow pattern, temperature

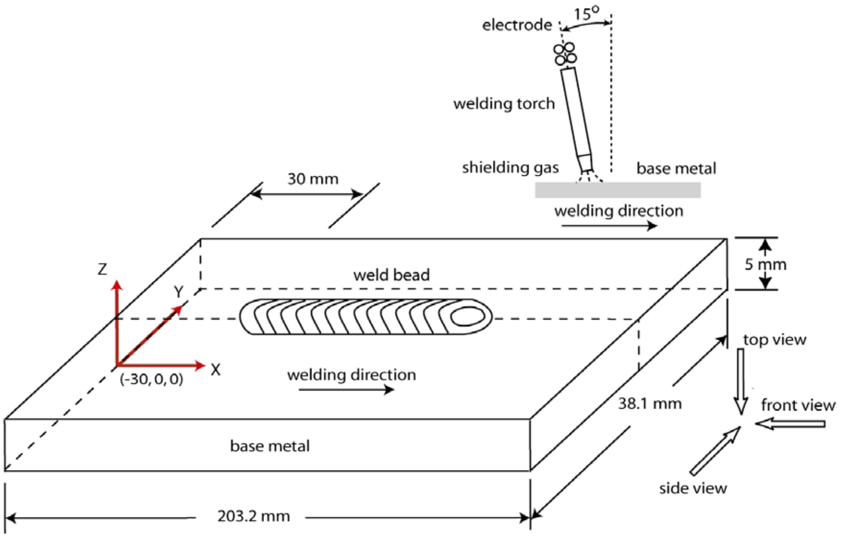

Fig. 2. Experimental setup and simulation domain of a GMAW system.

Table 2
Welding parameters.

	Time, t (s)	Current (A)	Voltage (V)	Wire feed speed (mm/s)	Welding speed (mm/s)
Normal crater	$t < 1.4$	183	23.5	69.8	14.8
	$t > 1.4$	0	0	0	0
Crater filling	$t < 1.4$	183	23.5	69.8	14.8
	$1.4 < t < 2.01$	82	23.5	0	−14.8

distribution, and the final weld bead shape were obtained. The welding parameters are shown in Table 2. Simulation is started when the welding arc is ignited at 30 mm to the left edge of the plate. To simulate a realistic welding process where the weld torch has a 15° lead angle and to account for the moving speed of the welding arc, the droplet also has a horizontal velocity in the arc moving direction in addition to the vertical velocity.

Fig. 3 shows a partial three-dimensional view of the simulated weld crater. Figs. 4 and 5 are the side and front views of the formation of the crater at the end of a welding process showing the weld bead shape change, temperature field, and velocity distribution. Before the arc is terminated at $t = 1.4$ s, it is observed that a weld pool has been formed with both the deposited hot material and the partially melted base metal. More metal is melted near the arc center because the arc heat flux is assumed to have a Gaussian distribution and the impinging droplets also carry energy into the molten pool. The weld pool surface is depressed under the effect of droplet impingement and arc pressure. Fluid flows downward at the arc center and, when reaching the weld pool bottom, flows upward and outward. As shown in Fig. 4(c), after the downward fluid flow reaches the weld pool bottom, part of the fluid flows upward to the left along the solid–liquid boundary and the rest flows upward to the right. The velocity of fluid to the left side decreases as it flows uphill, and when reaching the tail edge of the weld pool, the fluid solidifies and forms the top surface of the weld bead. The outward fluid flow can also be seen in Fig. 5(c), spreading the melted metal to both sides of the weld. A weld pool with a crater shaped surface is formed due to this flow pattern. Compared with the weld pool formed in the GMAW of steels [23,37], the thickness of the molten metal layer in the aluminum weld pool is thinner because of the faster solidification. While the weld pool moves to the positive x-direction with the arc center, it solidifies at the rear end and forms the weld bead.

At $t = 1.4$ s, the arc is terminated and there is no heat input and material transfer into the weld pool. The heat is transferred away from the weld pool via conduction to the bulk metal, convection between the liquid metal and air, and radiation loss to the surrounding environment. Compared with steel, because of its high thermal diffusivity, the aluminum weld pool cools down very fast and completely solidifies within a very short time of about 0.004 s. Since droplet impingement and the arc pressure do not exist anymore, there is no force at the arc center to depress the weld pool free surface and push the fluid to flow downward and then outward. The molten metal should tend to flow back under the gravity force. However, because the solidification is very fast, there is no time for the liquid to flow back and fill the crater. After the weld pool fully solidifies within 0.004 s, a weld bead is formed with a crater at the center.

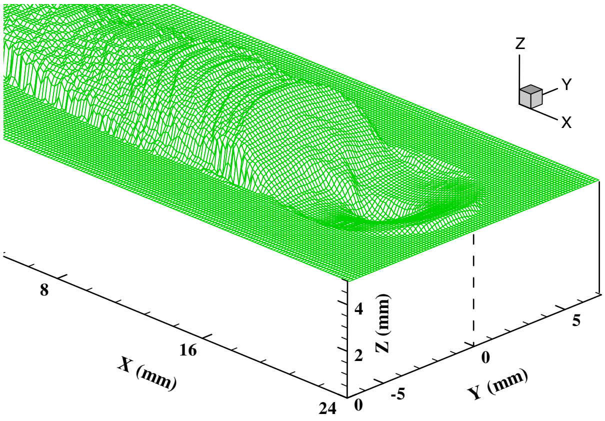

Fig. 3. Partial three-dimensional view of the simulated weld crater.

To validate the numerical model, experiments were performed for 1.4 s. The parameters were: current = 183 A, voltage = 23.5 V, wire feed speed = 69.8 mm/s, arc travel speed = 14.8 mm/s (Table 2). The base metal and resulting weld are shown in Fig. 6. The black zones in the base metal are Mg_2Si particles [41]. On the cross-section near the fusion line, the weld can be divided into three zones: fusion zone (FZ), where the metal was melted and then solidified; partial melted zone (PMZ), where the peak temperature is between the alloy's melting point and eutectic temperature; and heat-affected zone (HAZ), where no melting happened during welding but significant solid phase transformations took place. The FZ is characterized by columnar dendrites. The dark interdendritic network in the FZ is aluminum–silicon eutectic [41]. The PMZ has a coarse grain structure. In the HAZ near the weld bead, there are fewer Mg_2Si particles than in the base metal since near the weld bead the peak temperature is high enough for the particles to dissolve into the aluminum matrix. The cross-section of the weld bead of the crater at $x = 20$ mm is compared with simulated results in Fig. 7 and Table 3. From Fig. 7(a), a cracking through the middle of the weld bead is observed. It is believed that the crater cracking in GMAW of aluminum alloys belongs to solidification cracking [1,42]. The crack occurs during the terminal stage of solidification. The stresses are developed across the adjacent grains as a result of the base and weld metal contraction during solidification. When the stresses exceed the strength of the nearly completely solidified weld metal, the grains are pulled apart and solidification cracking is thus induced. As demonstrated in Fig. 7(b) and Table 3, a good agreement in weld dimensions between experimental and calculated results was obtained.

Knoop micro-hardness measurements were conducted on the base metal and weld bead. The average hardness is HK 82.17 with a standard deviation of HK 1.56 for the base metal and HK 54.25 with a standard deviation of HK 3.779 for the weld bead. Knoop hardness in the HAZ was measured on the $x = 30$ mm cross-section along a line 0.4 mm below the top surface of the welding sample (Fig. 8). The results are shown in Fig. 9. It is observed that although the measurement was performed after 1000 h of natural aging at room temperature, the hardness in the HAZ is still significantly lower than that of the base metal. Generally, the hardness increases when the distance to the fusion line increases. There is a significant hardness drop when the distance is less than 6 mm. The location of the lowest hardness is near 6 mm. Beside the low hardness zone and nearer to the fusion line, there is an increase in hardness, the peak of which is located between 3 mm and 4 mm. And then the hardness drops again when getting nearer to the fusion line. To explain the aforementioned micro-hardness variation phenomena, a graph of peak temperature along the hardness measurement line is presented in Fig. 9 and some metallurgical background information will be first introduced briefly.

The 6005 alloy used in this research is a heat-treatable aluminum alloy which gains its strength primarily through the formation of precipitates in the aluminum matrix during heat treatment. Four sequential precipitations may be formed in the alloy during the aging process. The finest one is called the GP zone, which has small disks a few atoms thick and less than 10 nm in

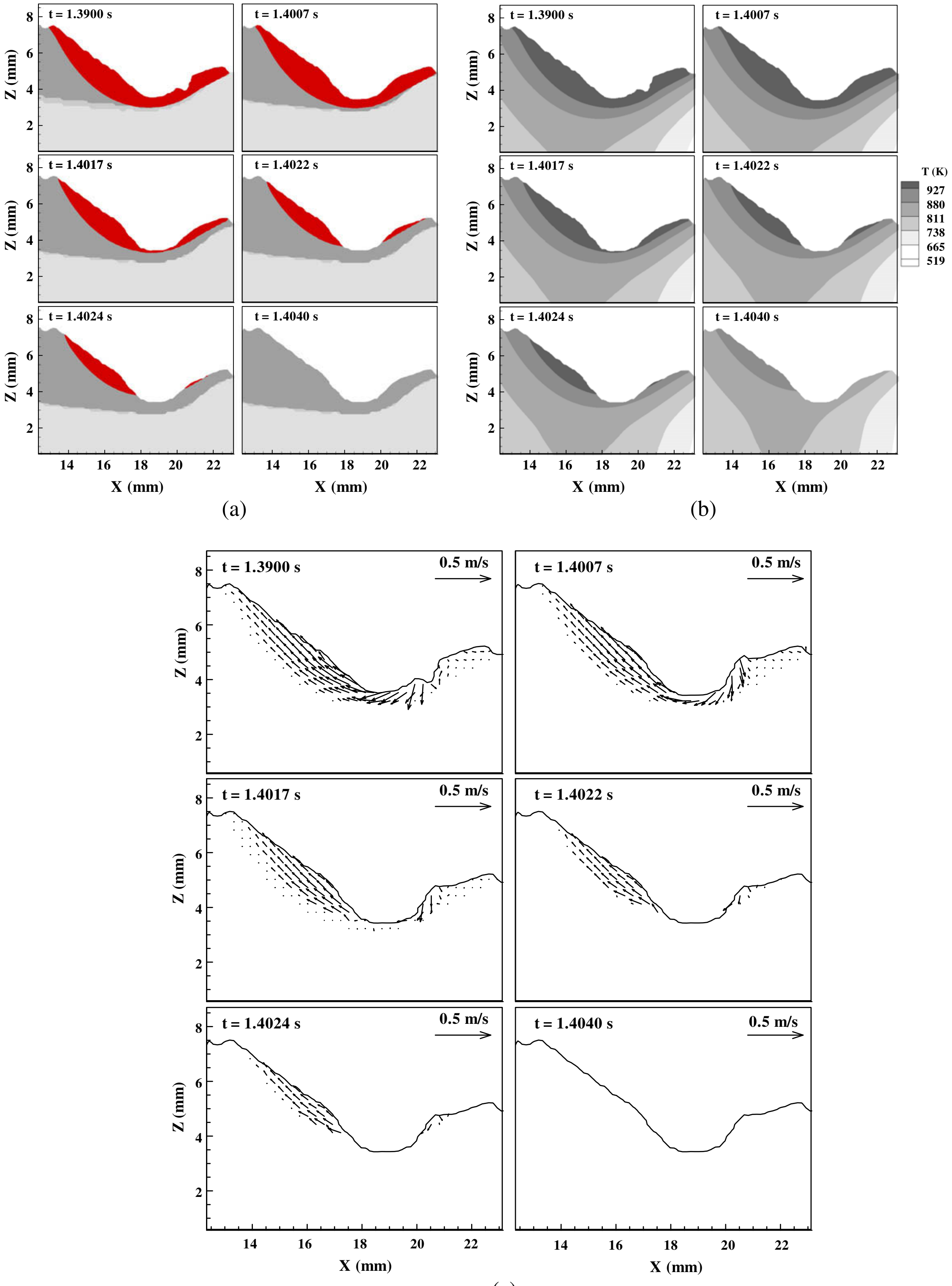

(a) (b)

(c)

Fig. 4. Side view of the formation of a crater: (a) weld pool (the darkest color) and weld bead (the second darkest color), (b) temperature field, and (c) velocity field.

diameter [42]. Further aging leads to the formation of the β″ phase, which is a needle-shaped precipitation larger than the GP zones. The next product of the aging process is the β′ Mg_2Si phase, which is formed from the β″ phase by growth in precipitate length and diameter [36]. The equilibrium phase β-Mg_2Si is formed in the final stage of aging by diffusionless transformation of the β′ phase. Among the four phases, GP zones and β′ phases have only moderate strengthening effects, and the contribution of the β phase is very small. β″ phase is the primary strengthening phase in 6xxx series alloys [43]. According to the research works of Malin [44], in the HAZ of the weld joint, the β″ phase begins to coarsen at temperatures below 523 K, which lowers the metal hardness. Further

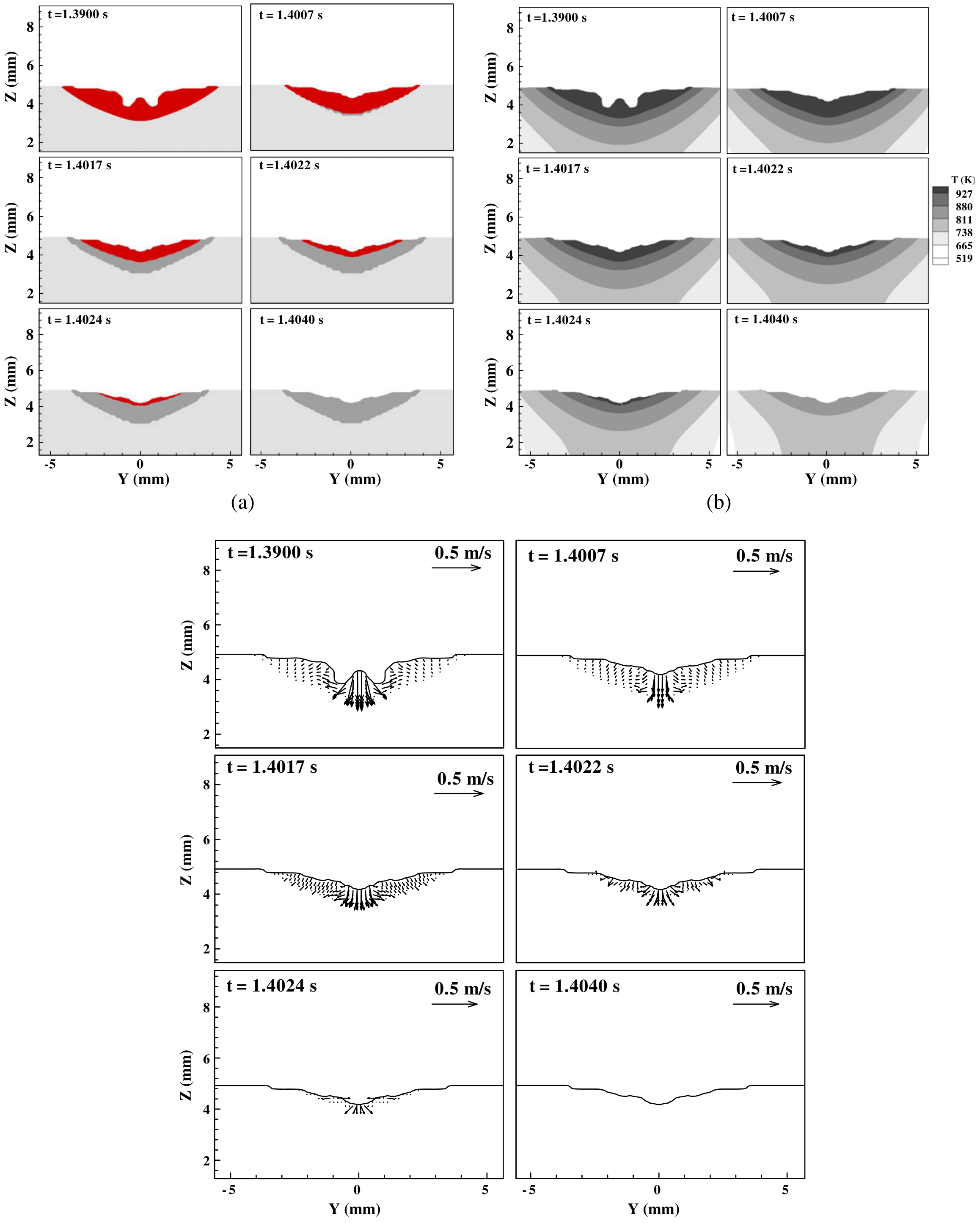

(a) (b)

(c)

Fig. 5. Front view of the formation of a crater: (a) weld pool (the darkest color) and weld bead (the second darkest color), (b) temperature field, and (c) velocity field.

increase of temperature causes the β″ phase to transform to the β′ phase between 523 K and 653 K. The β″ phase is reported to continue to coarsen in this temperature range [45]. When the temperature is elevated above 653 K, which is the solvus temperature of precipitations, both β″ and β′ phases dissolve in the aluminum matrix [45]. Although the composition of alloy in this research is different from the 6061 used by Dumolt [45] and Malin [44], according to Ceresara et al. [46], an excess of Mg or Si does not have any effect on the sequence and the structure of the normal precipitation process. Only the precipitation rate and extent are affected. The corresponding temperatures of 6005 alloy found by Maitland and Ried [47] are very close to the above data. Therefore, the temperatures organized by Malin [44] will be used as benchmarks for convenience.

It is observed from Fig. 9 that for the whole micro-hardness measurement zone, the peak temperature is above 523 K everywhere. When the temperature is between 523 K and 653 K, the β″ phase coarsens and also transforms to the β′ phase, causing low-

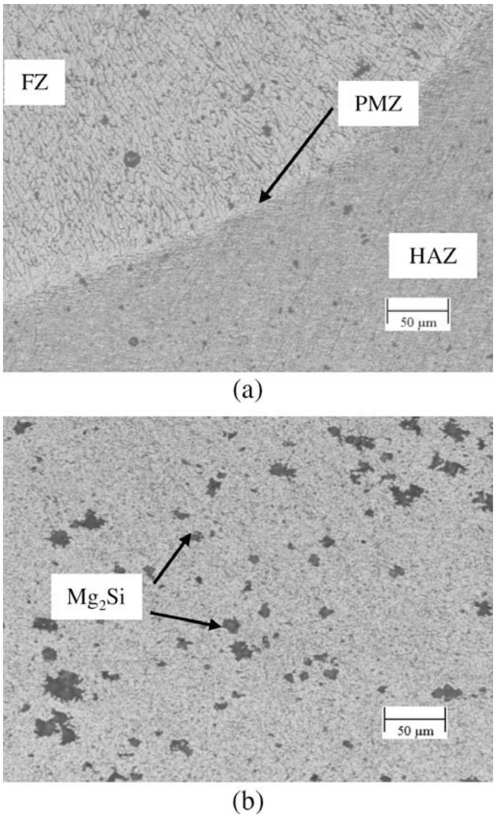

Fig. 6. Zones near the fusion line at the cross-section of the weld. (a) Zones near the fusion line and (b) base metal.

er hardness than that of the base metal. At 653 K, the size of the β″ phase and the amount of the β′ phase reach the maximum and the strength of the metal decreases to a minimum value [44]. This corresponds to the lowest hardness near 6 mm. In the region between 5.86 mm and 3.56 mm to the fusion line, where the temperature is between 653 K and 773 K, the dissolution of β″ and β′ occurs because the precipitations are held at temperatures higher than the solvus. The dissolution process enriches the solid solution of the aluminum matrix with alloying element Mg [45]. Therefore this zone may undergo a solution-hardening heat treatment during the heating and cooling of the welding process, which contributes to the rise of local hardness. Thus a local hardness increase is found at about 3.5 mm. Another contribution to the local hardness rise is that during the post-weld natural aging (>3000 h), new precipitates are formed, which can be either GP zones [47] or β″ phases. When the distance to the fusion line is less than 3.56 mm, the temperature is higher than 773 K. There are no precipitates in this zone because of the dissolution of β″ and β′ phases [45]. The aluminum matrix is therefore enriched with Mg. The possible reason for the hardness drop may be the diffusion of alloy element Mg between the solid and liquid metals at the interface between the weld pool and solid metal. In the electrode material 4043, the Mg content is far lower than in the base metal [40]. Since, during the welding process, areas adjacent to the fusion zone undergo high temperatures, the diffusion of Mg may not be negligible, inducing the depletion of Mg in this zone and consequently resulting in the hardness drop near the fusion line.

4.2. Crater filling

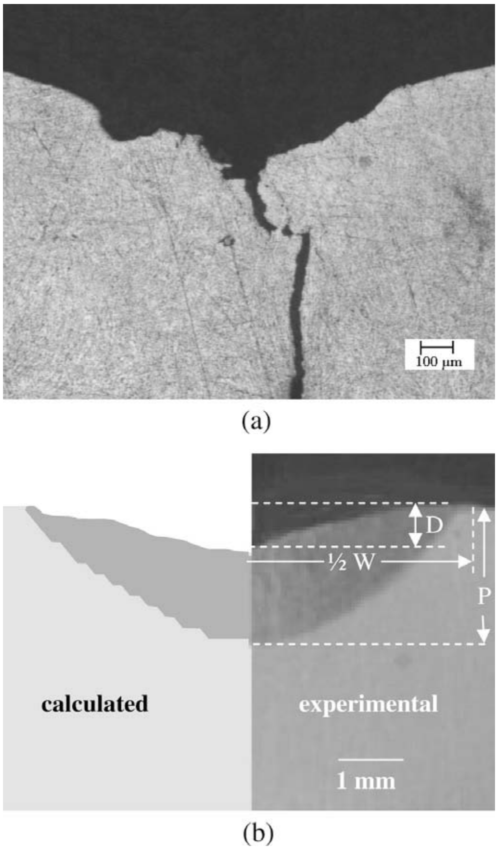

Fig. 7. Comparison of the experimental and calculated cross-sections for a crater at $x = 20$ mm. (a) Cracking at the crater center and (b) comparison of the results.

Table 3
Dimensions of cross-sections at $x = 20$ mm.

	Normal crater		Crater filling	
	Experiment	Simulation	Experiment	Simulation
P[b], mm	1.83[a]	1.89	1.97[a]	2.03
W[b], mm	7.38[a]	7.58	7.66[a]	7.80
D[b], mm	0.83[a]	0.92	–	–
R[b], mm	–	–	0.57[a]	0.51

[a] Average values are used for experimental results.
[b] P, penetration; W, width; D, crater depth; R, reinforcement.

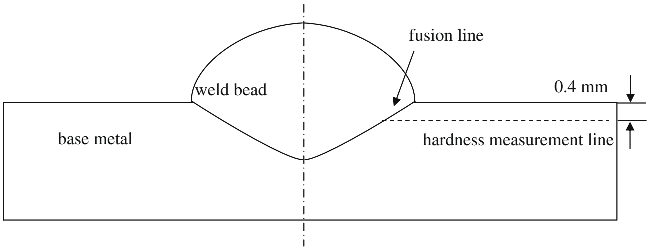

Fig. 8. Knoop hardness measurement positions.

One approach to reduce or even eliminate the existence of solidification cracking is to maintain a sufficient amount of molten metal during the terminal stage of solidification, which can flow into the cracking and thus fill and heal the cracks. To reduce the crater cracking of GMAW of aluminum alloys, it is desirable

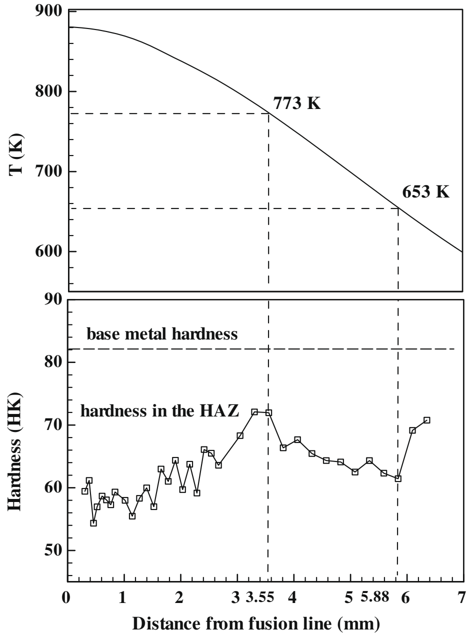

Fig. 9. Knoop hardness measurement results and peak temperature along the hardness measurement line on cross-section at $x = 20$ mm for a crater.

that the weld pool is kept longer at the final stage of welding to allow enough liquid metal to fill the cracking. Therefore, a "back-up" crater filling technique was employed in this research to maintain the weld pool and fill up the crater. The crater filling parameters are shown in Table 2. When $t < 1.4$ s, the normal welding parameters are used. When $t > 1.4$ s, a smaller set of parameters is used while the weld arc travel direction is reversed towards the left-hand side. There is only heat input from the welding arc after $t = 1.4$ s and no electrode material depositions. The crater filling procedure lasts for 0.6 s. The purpose is to fill the crater with small heat input to prevent unnecessary heat-affected zone (HAZ) softening. The change of welding current is shown in Fig. 10.

Fig. 11 is the side views of the simulated crater filling process showing the weld bead shape change, temperature field, and velocity distribution, respectively. When $t < 1.4$ s, the simulated results are the same as those of normal parameters. After $t = 1.4$ s, the arc travels in the negative x-direction and the welding current is reduced from 183 A to 83 A. In addition, there is no material deposition onto the workpiece. Since there is no droplet impingement and the arc pressure is also decreased significantly, the force driving the fluid to flow away from the arc center is vastly decreased. Therefore, under the influence of gravity, the liquid metal tends to flow back towards the center of the puddle and closes up the crater. At the beginning of the crater filling, e.g., at $t = 1.4190$ s, both fluid on the left-hand side and right-hand side of the arc center flow back. After colliding with each other at the center of the weld pool, the fluid flows upwards. With the arc moving to the negative x-direction, e.g., at $t = 1.4670$ s, the fluid on the right-hand side of the arc solidifies since it receives insufficient heat input. Only the left-hand side fluid flows downward to close up the crater. Because of the inertia of the metal, the liquid continues to flow upward to the right-hand side after reaching the bottom of the crater. The molten metal flowing to the right-hand side slows down near the right end of the weld pool, while at the same time at the left-hand side of the arc, "downhill" flowing liquid material still has significant momentum. Therefore, some fluid is pushed upward and piles up, forming a higher fluid level in the weld pool. Furthermore, as the arc proceeds to the left-hand side, e.g., at $t = 1.7070$ s, some previously solidified weld bead metal is re-melted, leading to an increase of the size of the weld pool. While the arc continues to move to the left-hand side, after a certain moment, the weld pool size begins to decrease. The arc is turned off at $t = 2.0$ s. At $t = 2.0040$ s, the weld pool has completely solidified.

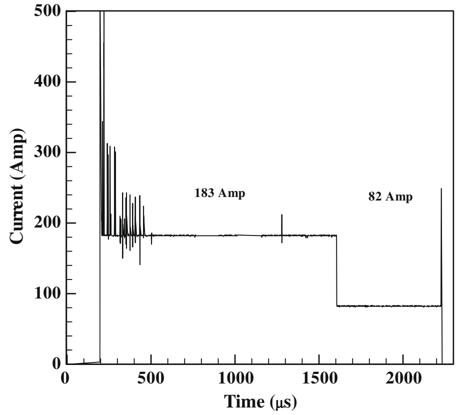

Fig. 10. Welding current in a crater filling technique.

Fig. 12 is the front views of the simulated crater filling process showing the weld bead shape change, temperature field, and velocity distributions at $x = 20$ mm, respectively. When the welding process enters the crater filling procedure by employing low current and no electrode material transportation, the driving force pushing liquid metal down at the arc center decreases significantly. After $t = 1.4$ s, due to the continuous heat input, the weld pool does not solidify immediately. Instead, it decreases gradually in size as the welding arc moves away from $x = 20$ mm. As the crater filling proceeds, e.g., at $t = 1.4270$ s, the liquid metal flows from the periphery back to the center, filling up the crater. The fluid velocity also decreases significantly. When the weld pool completely solidifies, a flat-top weld bead cross-section is formed, since there is no force pushing the weld pool center downward.

To validate the numerical model, experiments were performed for the crater-filling technique, the parameters of which are shown in Table 2. The cross-section of the weld bead of the filled-up crater at $x = 20$ mm is compared with the simulated results in Fig. 13 and Table 3. It is observed from Fig. 13(a) that there is no cracking in the weld bead. As demonstrated in Fig. 13(b) and Table 3, a good agreement in weld dimensions between the experimental and calculated results was obtained. Micro-hardness measurements were also conducted on crater-filling samples. The results are shown in Fig. 14. The hardness profile of the normal crater is also included for easy comparison. The peak temperature along the hardness measurement line was calculated in the model and is presented in Fig. 14. Compared with the normal crater, the positions corresponding to temperatures 653 K and 773 K are 6.31 mm and 4.07 mm from the fusion line, respectively, instead of 5.8 mm and 3.56 mm. The wider high temperature zones led to a generally lower hardness in the filled crater since the coarsening of the β'' phase and its transformation to β' precipitates are more serious when held at higher temperatures for a longer time. The filled crater hardness shows a similar trend to that of a normal crater. There is a significant hardness drop when the distance from the fusion line is between 6 mm and 7 mm. The lowest hardness is found around 6 mm. Beside the low hardness zone and nearer to the fusion line, there is an increase in hardness, the peak of which is near 4 mm. And then the hardness drops again toward the fusion line. The relationship between the hardness profile and peak temperature and the

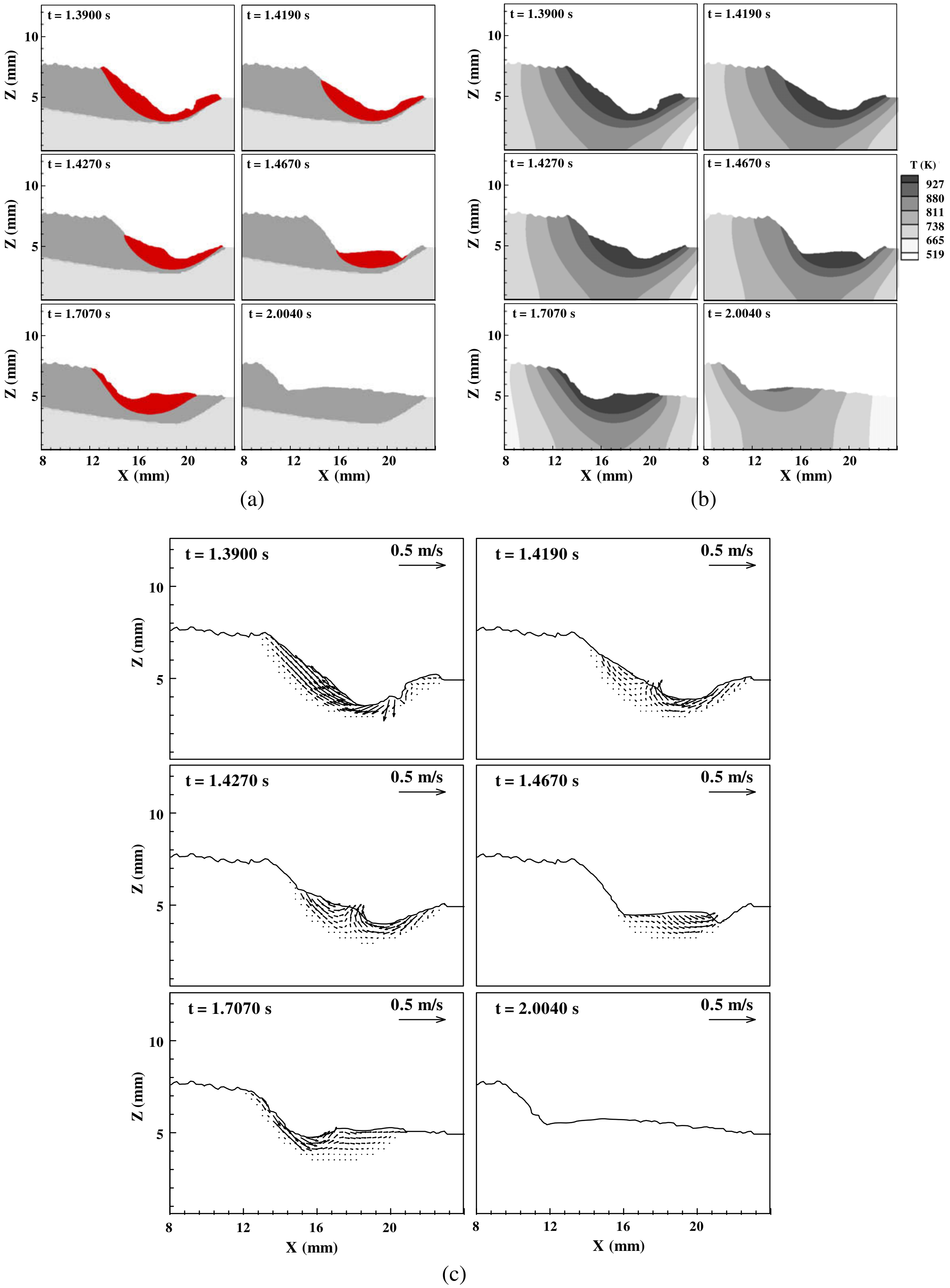

(a)

(b)

(c)

Fig. 11. Side view of the crater filling: (a) weld pool (the darkest color) and weld bead (the second darkest color), (b) temperature field, and (c) velocity field.

mechanisms are similar to those of the normal crater and will not be repeated here.

5. Conclusions

The fluid flow and heat and mass transfer in the weld pool for a moving GMAW of aluminum alloy 6005 were analyzed using the VOF technique and the continuum formulation. Weld pool and weld bead shapes, temperature field, and velocity distribution were obtained for the terminating stage of the welding process. Experiments were conducted on the formation of the stopping end of the weld. Metallurgical characterizations were performed on the welded samples. It was found that the crater is formed because of the depression at the weld pool center as a result of

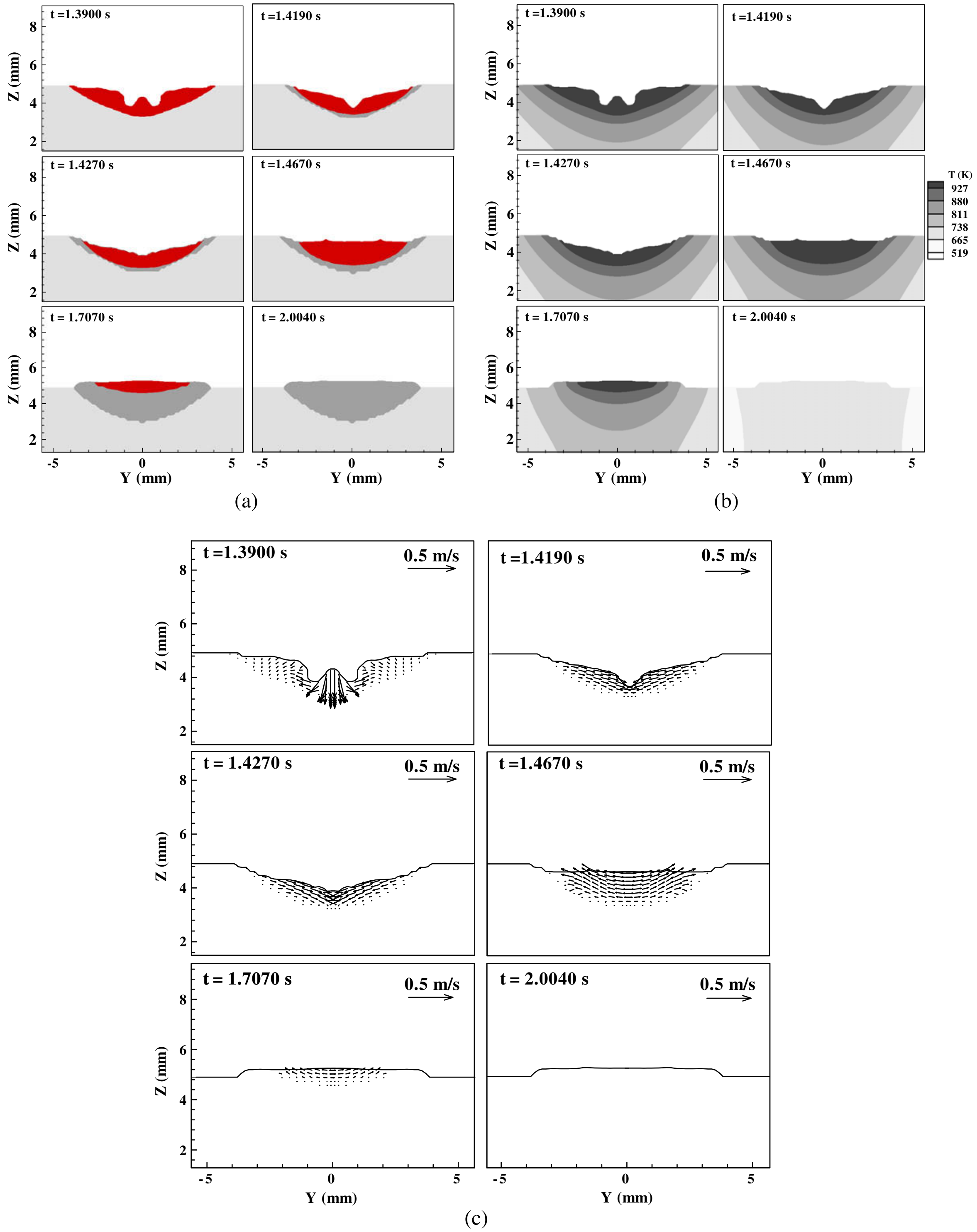

Fig. 12. Cross-sectional view at $x = 20$ mm of the crater filling: (a) weld pool (the darkest color) and weld bead (the second darkest color), (b) temperature field, and (c) velocity field.

droplet impingement effect and arc pressure. The weld pool solidifies very quickly once the weld process stops. Due to the rapid heat dissipation, there is no time for the molten metal to flow back towards the weld pool center and close up the crater. Thus, a crater is formed at the end of the weld bead. Solidification cracking is also formed at the center of the weld crater due to the fast solidification. To fill the crater and eliminate the cracking, a “back-up” crater filling technique was proposed. During the crater filling stage, the welding procedure switches from normal parameters to a smaller current for 0.6 s. At the same time, the welding arc moving direction is reversed. As a result, the weld pool is maintained for a longer time, and while its size decreases gradually, the crater is successfully filled and no cracking was found on the crater-filling experimental results.

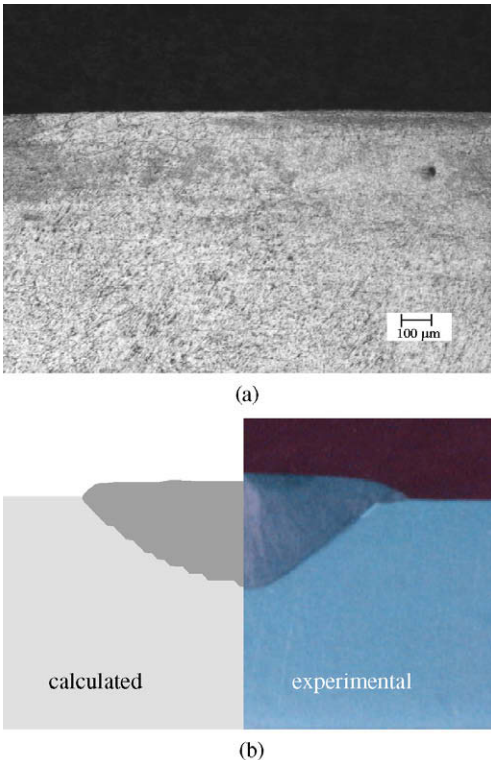

(a)

(b)

Fig. 13. Comparison of the experimental and calculated cross-sections for a filled crater at $x = 20$ mm: (a) center of the filled-up crater and (b) comparison of the results.

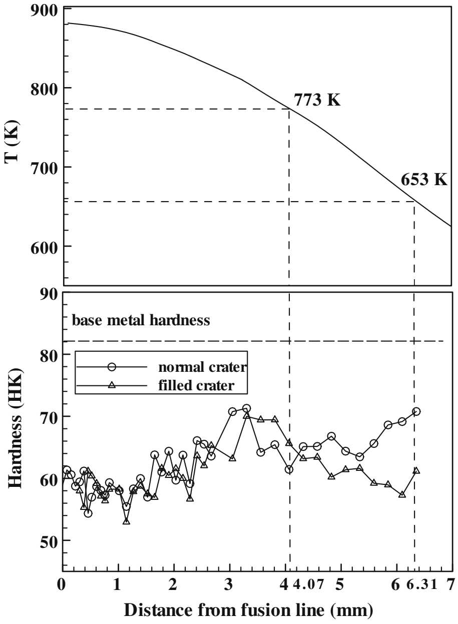

Fig. 14. Knoop hardness measurement results and peak temperature along the hardness measurement line on $x = 20$ mm cross-section for a crater filling.

References

[1] H.L. Saunders, Welding Aluminum: Theory and Practice, 3rd ed., The Aluminum Association, 1997, pp. 1.2–9.5.

[2] P.B. Dickerson, Weld discontinuities – causes and cures, Weld. J. 77 (6) (1998) 37–42.

[3] P. Dickerson, Quality control in aluminum arc welding, in: Proceedings of the Aluminum Joining Seminar Aluminum Association, Washington, DC, Landmark Motor Hotel, Metarie, Louisiana, 1986, pp. 331–359.

[4] O. Runnerstam, K. Persson, The importance of a good quality gas shield, Svetsaren 50 (3) (1995) 24–27.

[5] M. Pereira, C. Taniguchi, S. Brandi, S. Machida, Analysis of solidification cracks in welds of Al–Mg–Si A6351 type alloy welded by high frequency pulsed TIG process, Q. J. Jpn. Weld. Soc. 12 (3) (1994) 342–350.

[6] H. Kerr, M. Katoh, Investigation of heat-affected zone cracking of GMA welds of Al–Mg–Si alloys using the varestraint test, Weld. J. 66 (9) (1987) 251s–259s.

[7] Z. Lu, W. Evans, J. Praker, S. Birley, Simulation of microstructure and liquation cracking in 7017 aluminum alloy, Mater. Sci. Eng. A 220 (1996) 1–7.

[8] M. Mizuno, S. Takeno, T. Teramoto, Y. Sakei, Relations between restraint intensity and weld cracking in welding of aluminium alloy, in: Proceedings of the Third International Conference Aluminium-Verlag, Duesseldorf, Munich, FRG, 1985, pp. I.5.1–I.5.13.

[9] E.C. Partington, Control of metal transfer in modulated pulse M.I.G. welding, in: IIW Asian Pacific Regional Welding Congress, 1988, pp. 970–988.

[10] A.J. Sunwoo, E.L. Bradley III, J.W. Morris Jr., Effects of heat-affected zone peak temperature on the microstructure and properties of 2090 Al alloy, Metall. Trans. A 21A (10) (1990) 2795–2804.

[11] L.A. Guittnerez, G. Neye, E. Zschech, Microstructure, hardness profile and tensile strength in welds of AA6013 T6 extrusions, Weld. J. 75 (4) (1996) 115s–121s.

[12] M.J. Lu, S. Kou, Power inputs in gas metal arc welding of aluminum – part 1, Weld. J. 68 (9) (1989) 382s–388s.

[13] A.O. Kluken, B. Bjorneklett, A study of mechanical properties for aluminum GMA weldments, Weld. J. 76 (2) (1997) 39–44.

[14] T. Ma, G. Ouden, Heat-affected zone softening during arc welding of Al–Zn–Mg alloys, Int. J. Join. Mater. 8 (3) (1996) 105–110.

[15] R.P. Martukanitz, C.A. Natalie, J.O. Knoefel, The weldability of an Al–Li–Cu alloy, J. Met. 39 (11) (1987) 38–42.

[16] V.P. Budnik, Effect of the type of inert gas on pool temperature and fracture of the oxide film in welding aluminium, Paton Weld. J. 6 (12) (1994) 23–25.

[17] J. Domey, D.K. Aidun, G. Ahmadi, L.L. Regel, W.R. Wilcox, Numerical simulation of the effect of gravity on weld pool shape, Weld. J. 74 (8) (1995) 263s–268s.

[18] W.H. Kim, H.G. Fan, S.J. Na, Effect of various driving forces on heat and mass transfer in arc welding, Numer. Heat Transfer A 32 (1997) 633–652.

[19] K. Hong, D.C. Weckman, A.B. Strong, The influence of thermofluids phenomena in gas tungsten arc welds in high and low thermal conductivity metals, Can. Metall. Q. 37 (3–4) (1998) 303–393.

[20] Y. Wang, Q. Shi, H.L. Tsai, Modeling of the effects of surface-active elements on flow patterns and weld penetration, Metall. Mater. Trans. B 32B (2) (2001) 145–161.

[21] R.T.C. Choo, J. Szekely, R.C. Westhoff, On the calculation of the free surface temperature of gas-tungsten-arc weld pools from first principles. Part I. Modeling the weld arc, Metall. Trans. B 23B (6) (1992) 357–369.

[22] R.T.C. Choo, J. Szekely, S.A. David, On the calculation of the free surface temperature of gas-tungsten-arc weld pools from first principles. Part II. Modeling the weld pool and comparison with experiments, Metall. Trans. B 23B (6) (1992) 371–384.

[23] Y. Wang, H.L. Tsai, Impingement of filler droplets and weld pool dynamics during gas metal arc welding process, Int. J. Heat Mass Transfer 44 (2001) 2067–2080.

[24] S.-Y. Lee, S.-J. Na, A numerical analysis of a stationary gas tungsten welding arc considering various electrode angles, Weld. J. 75 (9) (1996) 259s–269s.

[25] M. Ushio, C.S. Wu, Mathematical modeling of three-dimensional heat and fluid flow in a moving gas metal arc weld pool, Metall. Mater. Trans. B 28B (6) (1995) 509–516.

[26] J. Jaidi, P. Dutta, Modeling of transport phenomena in a gas metal arc welding process, Numer. Heat Transfer A 40 (2001) 543–562.

[27] H. Park, S. Rhee, Analysis of weld geometry considering the transferring droplets in gas metal arc welding, JSME Int. J. Ser. C 44 (3) (2001) 856–862.

[28] M.H. Davies, M. Wahab, M.J. Painter, An investigation of the interaction of a molten droplet with a liquid weld pool surface: a computational and experimental approach, Weld. J. 79 (1) (2000) 18s–23s.

[29] V.K. Arghode, A. Kumar, S. Sundarraj, P. Dutta, Computational modeling of GMAW process for joining dissimiliar aluminum alloys, Numer. Heat Transfer A 53 (4) (2008) 432–455.

[30] J. Hu, H.L. Tsai, Heat and mass transfer in gas metal arc welding. Part I. The arc, Int. J. Heat Mass Transfer 50 (2007) 833–846.

[31] J. Hu, H.L. Tsai, Heat and mass transfer in gas metal arc welding. Part II. The metal, Int. J. Heat Mass Transfer 50 (2007) 808–820.

[32] J. Hu, H.L. Tsai, Effects of current on droplet generation and arc plasma in gas metal arc welding, J. Appl. Phys. 100 (2006) 053304.

[33] J. Hu, H.L. Tsai, Metal transfer and arc plasma in gas metal arc welding, ASME J. Heat Transfer 129 (2007) 1025–1035.

[34] D.B. Kothe, R.C. Mjolsness, M.D. Torrey, Ripple: A Computer Program for Incompressible Flows with Free Surfaces, LA-12007-MS, Los Alamos National Laboratory, 1991.

[35] Q.Z. Diao, H.L. Tsai, Modeling of solute redistribution in the mushy zone during solidification of aluminum–copper alloys, Metall. Trans. A 24A (4) (1993) 963–973.

[36] J.E. Hatch (Ed.), Aluminum: Properties and Physical Metallurgy, American Society for Metals, Metals Park, OH, 1984, pp. 13–19.

[37] J. Hu, H. Guo, H.L. Tsai, Weld pool dynamics and the formation of ripples in 3D gas metal arc welding, Int. J. Heat Mass Transfer 51 (2008) 2537–2552.

[38] T. Zacharia, S.A. David, J.M. Vitek, Effect of evaporation and temperature dependent material properties on weld pool development, Metall. Trans. B 22B (2) (1992) 233–241.

[39] S.V. Patankar, Numerical Heat Transfer and Fluid Flow, first ed., Hemisphere, New York, NY, 1980.

[40] ASM, Properties and Selection: Nonferrous Alloys and Pure Metals, 9th ed, Metals Handbook, vol. 2, American Society for Metals, Metals Park, OH, 1985, p. 113.

[41] ASM, Metallography and Microstructures, 9th ed, Metals Handbook, vol. 9, American Society for Metals, Metals Park, OH, 1985, pp. 352–354.

[42] S. Kou, Welding Metallurgy, Wiley, New York, 1987. p. 278.

[43] T. Enjo, T. Kuroda, Microstructure in weld heat-affected zone of Al–Mg–Si alloy, Trans. JWRI 11 (1) (1982) 61–66.

[44] V. Malin, Study of metallurgical phenomena in the HAZ of 6061-T6 aluminum welded joints, Weld. J. 74 (9) (1995) 305s–318s.

[45] S.D. Dumolt, Metallurgical Transformations in the Heat-Affected Zone of Aluminum Alloys by Transmission Electron Microscopy, Carnegie-Mellon University, Pittsburgh, PA, 1983.

[46] S. Ceresara, E. Di Russo, P. Fiorini, A. Giarda, Effect of Si excess on the aging behavior of Al–Mg_2–Si 0.8% alloy, Mater. Sci. Eng. 5 (1969–1970) 220–227.

[47] A.H. Maitland, A. Ried, Metallurgical events in the heat affected zone of AlMgSi alloys, in: International Aluminum Welding Conference, Cleveland, OH, 1981, pp. 106–114.